Structure and Reactivity of Ni−Au Nanoparticle Catalysts

Alfons M. Molenbroek* and Jens K. Nørskov

Center for Atomic-Scale Materials Physics, Technical University of Denmark, DK-2800 Lyngby, Denmark

Bjerne S. Clausen

Haldor Topsøe A/S, Nymøllevej 55, DK-2800 Lyngby, Denmark

Received: December 7, 2000; In Final Form: March 2, 2001

We discuss the design of a Ni−Au nanoparticle catalyst system, which is based on the detailed experimental and theoretical understanding of the alloying and the chemical reaction processes on single-crystal surfaces. The alloy formation and structure of Ni−Au catalysts supported on SiO_2 and on $MgAl_2O_4$ are simulated by Monte Carlo schemes as well as experimentally studied by a combination of in situ X-ray absorption fine structure, transmission electron microscopy, and in situ X-ray powder diffraction. On-line mass spectrometry is used to follow the reactivity of the catalyst and thermogravimetric analysis provided information on the deposition rate of carbon during steam reforming of *n*-butane. The simulations and the experiments give evidence for the formation of a Ni−Au surface alloy on the Ni particles for both supports. The Ni−Au catalysts exhibiting the surface alloy are active for steam reforming and are more resistant toward carbon formation than the pure Ni catalyst. Blocking of highly reactive Ni edge and kink sites by Au atoms is presumably the reason for the increased robustness of the Ni−Au catalyst.

1. Introduction

It has long been appreciated that alloys may possess special structural and catalytic properties compared to the pure alloy constituents (see, e.g., refs 1 and 2). The application of bimetallic catalysts in industry has been considerable, notably within the petroleum industry for catalytic reforming of petroleum fractions, but alloys are also used for environmental applications such as car exhaust catalysts. Since changing the alloy composition can vary the chemical reactivity, it is expected that catalysts for several new applications will be based on alloy systems. The understanding of bimetallic clusters was previously impeded by the lack of suitable physical methods and the insight into these catalysts was mainly obtained from probing the catalytic activity. With the development of extended X-ray absorption fine structure (EXAFS),[3] researchers have obtained a tool which is particularly well suited for the investigation of highly dispersed bimetallic clusters and important results on their catalyst structure have appeared.[4] Notably, it has been found that bimetallic systems of interest to catalysis are not limited to combinations of metallic elements that are highly miscible in the bulk. For example, the ruthenium−copper system, in which the two components are virtually completely immiscible in the bulk, exhibits selective inhibition of hydrogenolysis similar to that observed with the completely miscible nickel−copper system.[5,6] It was concluded that a new catalyst was created with structural and bonding properties that are not directly related to a simple combination of the constituents.

The bulk binary phase diagram of Au and Ni has a large miscibility gap, thus no alloy is formed at low temperatures.[7] However, it has been found by STM that deposition of Au on Ni(110) or Ni(111) single-crystal surfaces can result in a stable surface alloy in the first atomic layer.[8,9] Low energy ion scattering in combination with low energy electron diffraction of Au on Ni(110) has also shown the formation of a surface alloy restricted to the outermost atomic layer.[10] Total energy calculations using the effective medium theory[8,11] and later based on density functional theory[12] confirmed that the formation of a surface alloy of Au on Ni(110) and Ni(111) is energetically favorable. The alloy formation of Au into the surface of a Ni(110) or Ni(111) single crystal not only influences the structural properties of the surface but influences the chemical properties as well. Molecular beam experiments using seeded supersonic methane beams showed that the reactivity toward methane decomposition is reduced by alloying Au into the surface of Ni(111).[13] Calculations using density functional theory have shown that the dissociation barrier for the removal of the first hydrogen atom from CH_4 increases significantly in the presence of Au in the Ni(111) surface.[14] The increase in dissociation barrier for the dissociative adsorption of CH_4 was attributed to electronic effects, i.e. a downshift in the local density of Ni d-states by the presence of neighboring Au atoms.[14,15]

On the basis of these results and a fundamental knowledge of the segregation and chemical reaction processes at the surface, a bimetallic Ni−Au catalyst was designed, which shows the expected resistance toward carbon formation in the steam reforming process.[16,17] This result is of great interest since it is one of the first examples where it was possible to design a technical catalyst from surface science studies and knowledge of fundamental surface properties.

In this paper, we describe in detail how Monte Carlo simulations and various physicochemical characterization tools are used to get information on the existence of the Ni−Au surface alloy in the small particle system encountered in the supported catalysts. The catalysts are characterized structurally by means of transmission electron microscopy (TEM), in situ extended X-ray absorption fine structure measurements (EXAFS), and X-ray powder diffraction (XRPD). The catalytic

* Corresponding author. Present address: Haldor Topsøe A/S, DK-2800 Lyngby, Denmark. E-mail: am@topsoe.dk. Fax: 0045 4527 2999.

10.1021/jp0043975 CCC: $20.00
Published on Web 05/18/2001

TABLE 1: Overview of Sample Compositions, Supports, and Transmission Electron Microscopy (TEM) Results

sample	support	Ni loading (wt %)	Au loading (wt %)	Ni/Au (mol/mol)	particle size[a] (nm)
1	SiO_2	5.07			3.0−7.0
2	SiO_2	4.90	0.43	38.3	2.5−6.0
3	SiO_2	4.36	0.83	17.6	
4	SiO_2	8.5	1.04	28.5	
5	$MgAl_2O_4$	16.8			
6	$MgAl_2O_4$	16.4	0.30	182	3.0−15.0
7	$MgAl_2O_4$	15.5	0.24	215	3.0−10.0, some up to 50.0

[a] Estimated from TEM.

activity is measured by means of on-line mass spectrometry (MS) in connection with the EXAFS experiments. Catalyst deactivation due to carbon deposition is studied in separate experiments by thermogravimetric analysis (TGA).

2. Experimental Section

2.1 Sample Preparation. Monometallic Ni catalysts were prepared on SiO_2 and $MgAl_2O_4$ (mixed with α-Al_2O_3) high surface area supports with a total Ni loading between 5 and 16 wt %. The Ni−$MgAl_2O_4$ catalyst were prepared by pore filling of the spinel carrier with Ni-nitrate, whereas the Ni−SiO_2 catalyst was prepared using the precipitation-deposition method.[18] The bimetallic Ni−Au catalysts were prepared by careful impregnating the reduced monometallic Ni catalysts with an aqueous solution containing $Au(NH_3)_4(NO_3)_3$. After filtering, the product was dried in air at 383 K. Catalysts with a Ni−Au molar ratio varying by a factor of 6 were prepared (see Table 1).

2.2. Monte Carlo Simulations. Monte Carlo simulations were performed on nanometer sized Ni−Au clusters employing the effective medium theory (EMT)[19] to describe the interactions between Ni and Au atoms. The EMT is known to describe reasonably the experimental data obtained at Ni single-crystal surfaces with Au alloyed in the outermost atomic layer.[8,11,20] For the Ni(100) and the Ni(110) surfaces a Ni−Au surface alloy is energetically more stable than a Au overlayer, whereas the energy difference between a surface alloy and a Au overlayer on the Ni(111) surface is rather small. In the latter case entropy effects favor the disordered surface alloy.

The alloying behavior of small Ni−Au particles is studied using Monte Carlo simulations with exactly the same potentials as in the slab calculations referenced above. The simulations were performed as described previously.[21] In short, a spherically truncated fcc crystallite, with Au and Ni atoms placed randomly at lattice sites, is chosen as a starting configuration for the simulations. The chosen shape is in reasonable agreement with TEM observations of supported particles (see TEM results below). The lattice constant is chosen as a linear interpolation with respect to the Ni/Au atomic ratio of the Ni and Au bulk lattice constants. The Ni/Au atomic ratios are chosen in the range $[1,\infty]$, the temperature is fixed at 300 K (to compare the simulations to experimental results obtained at room temperature) and the total number of atoms in the cluster is varied in the range [55,1505]. The Monte Carlo scheme allows for two types of trial moves: the labels of two atoms can be swapped and the total volume of the cluster can be changed isotropically. The clusters are equilibrated typically within 500 Monte Carlo cycles. In one cycle the labels of all atoms in the cluster are attempted to swap with a randomly chosen atom label in the cluster and a volume change is attempted.

After equilibration of the clusters, parameters such as partial coordination numbers (N_{AuAu}, N_{AuNi}, N_{NiAu}, and N_{NiNi}), average interatomic distances (R_{AuAu}, $R_{AuNi} = R_{NiAu}$, and R_{NiNi}) and vibration amplitudes are obtained over a series of statistically independent snapshots.

2.3. XAFS Calculations. XAFS calculations were performed on model Ni and Ni−Au systems using the FEFF 8.00 code to compute the absorption spectra.[22,23] To test the overall accuracy of the calculations, the code is first used to compute the EXAFS signals for bulk fcc Ni and Au at the Ni K-edge and the Au L_3-edge, respectively. The Debye model in the FEFF code is used to calculate the Debye−Waller factors using a temperature of 300 K and Debye temperatures of $\Theta_{Ni} = 427$ K and $\Theta_{Au} = 185$ K. The Hedin−Lunqvist model is used to adjust the exchange correlation potential using the constant shifts of the Fermi level of $\Delta E_{0,Ni} = 5.0$ eV and $\Delta E_{0,Au} = 1.5$ eV. A uniform decay (imaginary part of the exchange parameter) was added to get a better agreement between measured and calculated data. Values of 3.0 and −1.0 are used for Ni and Au. Atoms are placed on bulk lattice positions using the lattice constants $a_{Ni} = 0.3524$ nm, $a_{Au} = 0.4078$ nm. The maximum effective half-path distance of the scattering paths is limited to 0.70 nm. All other parameters used as input for the EXAFS calculations are the default program values.

The effect of the particle size on the XAFS signal and its Fourier transform is calculated by placing Ni atoms on bulk fcc positions in a spherically truncated cluster. The total absorption is obtained by calculating the absorption for every atom in the cluster and averaging the total signal by use of the "cfaverage" parameter in the FEFF code. The Debye model is used to take the finite temperature into account. All the parameters in the input file are chosen identical to the ones used for the bulk simulation in the previous section.

The influence of alloying Au with Ni on the EXAFS signals is obtained by calculating the EXAFS signals on several types of Ni−Au nanoparticle alloys for several sizes and atomic ratios of the constituents. Ni and Au atoms are placed on a fcc spherically truncated lattice. Au atoms are placed at the surface and Ni atoms in the center of a cluster in accordance with the results of the Monte Carlo simulations. The lattice constant of the cluster is chosen as the weighted average of the lattice constant of bulk Ni and bulk Au, so it is dependent on the Ni/Au ratio. The Debye model with bulk Debye temperatures is used to calculate thermal vibrations.

2.4. Transmission Electron Microscopy. Transmission electron microscopy (TEM) measurements were performed on samples that were reduced for 1 h in hydrogen at 823 K and then passivated gently by slowly increasing the content of oxygen in the gas flow at room temperature. The microscope used was a Philips EM430 operated at 300 kV. X-ray micro-analysis using an energy dispersive spectrometer (EDS) was carried out on a series of particles present on the TEM pictures in order to determine the local Ni/Au atomic ratio.

2.5. X-ray Diffraction. An XRPD setup in the Debye−Scherrer geometry was used to perform in situ powder diffraction measurements on the Ni and Ni−Au supported samples. The incoming Cu Kα radiation was monochromatized by a double crystal Si(111) monochromator and collimated to a spot size of approximately 0.7×8 mm at the sample. The sample was enclosed in a quartz capillary tube (diameter: 0.7 mm, wall thickness: 0.01 mm) and connected to a gas handling system with pressure and flow controllers (see ref 24 for a detailed description). The tube was heated by means of a constant flow of hot nitrogen. A thin graphite foil covered the tube in order

to obtain a homogeneous temperature over the entire sample. The XRPD patterns were collected by a one-dimensional position sensitive detector (INEL CPS120), which allows for the simultaneous collection of a diffractogram over an angular range of 120° with an angular accuracy of 0.03°. The sample was reduced in pure hydrogen to 850 K (at a pressure of 1.8 bar and a flow of 15 N ml/min), and XRPD diagrams were collected before and during heating. After reduction for 2 h at 850 K, the sample was cooled to room temperature in hydrogen and a diagram with good statistics was collected.

2.6. EXAFS Experiments. EXAFS experiments were performed at the RÖMO II beamline at HASYLAB at DESY (Hamburg) and at the BL18 beamline at the ESRF (Grenoble), using Si(111) and Si(311) double-crystal monochromators. The monochromator was detuned to about 60% of the maximum intensity to reduce the amount of higher harmonics in the beam. Flow-ionization chambers filled with nitrogen or argon were used to measure the X-ray intensity in front of and behind the sample and behind a reference sample. The sample was crushed and a sieved fraction with particle diameters in the range 0.15−0.30 mm was loaded between graphite foils in an in situ EXAFS cell[25] which allowed for heating in different gas flows. X-ray absorption spectra were collected at the Ni K-edge and the Au L_3-edge. The X-ray absorption data were analyzed by standard procedures (see e.g. ref 26). In short, the EXAFS signals were extracted from the absorption spectra by subtracting the background followed by determination of the edge energy E_0, the jump height, and normalization of the spectrum. The energy scale was transformed to a momentum scale, glitches were removed and the k range was reduced to the interval 25−150 nm^{-1}. Spline fitting techniques using five equidistantly spaced intervals and cubic splines (except for the first interval for which a quadratic spline was chosen) were used to simulate the atomic absorption. The EXAFS signal was obtained by subtracting the atomic background and multiplication by k^1 or k^3 in order to obtain an evenly distributed amplitude of the signal. The spectrum was Fourier transformed and the first shell was filtered by means of a cosine-square filter and Fourier back-transformed. The resulting back-transformed spectra were fitted to Ni and Au amplitude and phase functions experimentally obtained from Ni and Au reference foils. Coordination numbers N, interatomic distances R, and Debye−Waller factors σ were obtained in the multiparameter fit, in which E_0 was varied as well.

2.7. Combined Reactivity and EXAFS Measurements. A Baltzer Thermostar mass spectrometer was connected to the outlet of the reaction cell. After reduction in pure hydrogen at 850 K for 1 h, the catalyst was exposed to a mixture of 3 vol % *n*-butane, 7 vol % hydrogen, and 3 vol % water in helium at 473 K. The water concentration was obtained by saturating the *n*-butane/H_2/He gas mixture with purified water at room temperature. A bypass system was used to flush the gas tubes before exposing the catalyst to the reaction mixture. QEXAFS and MS spectra were collected simultaneously during steam reforming of *n*-butane. The temperature was slowly increased (heating ramp, 5 K/min) to 823 K and kept there for 2 h. After steam reforming, the sample was cooled to room temperature and good quality XAFS spectra were collected at the Ni K-edge and the Au L_3-edge.

2.8. Thermogravimetric Analysis (TGA). A Cahn microbalance was used to measure the weight increase of the Ni−Au and Ni catalysts during steam reforming of *n*-butane. The TGA measurements were performed after reducing the samples in pure hydrogen to a temperature of 873 K for 1 h. After reduction, the reactor was evacuated to below 0.05 mbar at a temperature of 723 K, flushed with hydrogen, and exposed to the steam-reforming gas mixture (*n*-butane/H_2/He/H_2O) with the same composition as used for the XAFS measurements. After equilibration for 3 h, the sample was heated with 0.5 K/min to 823 K and the weight increase was measured as the increase in percent at this temperature with respect to the starting weight. Experiments were performed on fresh catalysts for several steam/carbon (O/C) ratios of the gas mixture, in the range [0.2,1.1], by diluting with He.

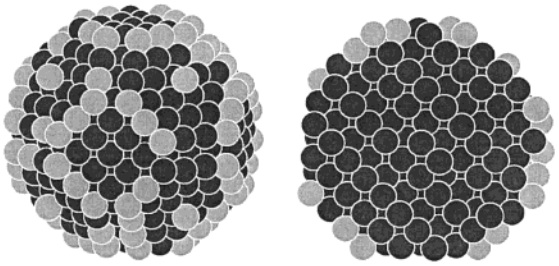

Figure 1. Snapshot of a Ni−Au nanoparticle after equilibration in a MC-scheme at 300 K. The particle consists of 100 Au atoms (light) and 583 Ni atoms (dark) with an outer diameter of 2.6 nm. Left: projected snapshot of the Ni−Au particle with Au present as a surface alloy at the surface of the Ni cluster. Right: snapshot sliced through the center of the particle.

3. Results

3.1. Monte Carlo Simulations. Figure 1 shows one example of the result of a Monte Carlo simulation for a Ni−Au catalyst particle consisting of 583 Ni atoms and 100 Au atoms. Similar results were obtained for higher Ni/Au concentrations. It is clearly seen that the Au atoms are exclusively located at positions at the surface of the small Ni particle. The Au atoms preferentially move to the edge and kink sites between the low-index planes of the Ni (the low energy (110) facets) giving an average coordination number around Au of five Ni atoms. No Au atoms are present in the "bulk" part of the cluster. No clustering of the Au atoms is observed up to the maximum studied particle size of 3.5 nm.

3.2. XAFS Calculations. Figure 2 shows the k^1-weighted amplitudes of the Fourier transformed FEFF-calculated XAFS spectra of bulk Au and bulk Ni as obtained after a standard analysis. Experimental data for Ni and Au reference foils are shown for comparison. The calculated spectra agree quantitatively with the experimental data, indicating that the FEFF calculations combined with the Debye model give a good description of the XAFS for bulk Ni and Au. Figure 3 shows the calculated XAFS signals and the corresponding magnitudes of the Fourier transformed spectra for various Ni cluster sizes: 0.7 nm (13 atoms), 1.1 nm (55 atoms), and 1.8 nm (249 atoms) and for bulk Ni. The magnitude of the Fourier transform decreases with decreasing particle size and the decrease is largest for atomic shells at large distances. This is well-known from standard EXAFS theory as the magnitude of a peak in the Fourier transformed spectrum, due to a single scattering contribution, scales roughly with the coordination number, the latter being a measure of the particle size.

The upper part of Figure 4 shows the Ni K-edge Fourier transformed spectra for four Ni−Au clusters with different Ni/Au ratios (0.5, 1.0, 2.0, and 10.0) and a total number of 249 atoms at $T = 300$ K. The data resemble the spectra of bulk Ni relatively well (compare to Figure 2). The shift of the different coordination shells to higher r values for lower Ni/Au ratios is due to the larger interatomic distance chosen for these clusters.

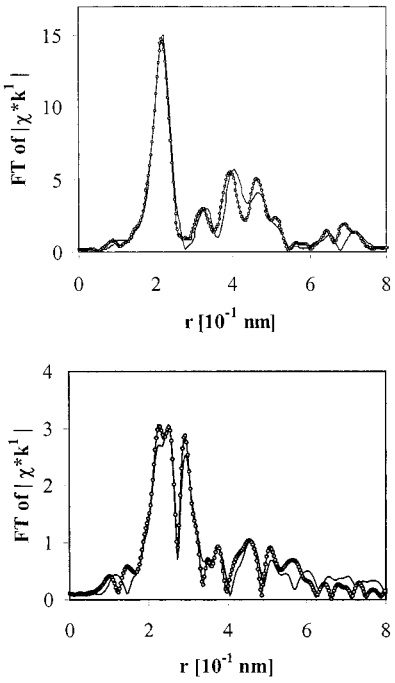

Figure 2. Calculated (curve with dots) and experimental (solid curve) magnitudes of the k^1-weighted Fourier transformed XAFS spectra of bulk Ni (upper diagram) and bulk Au (lower diagram).

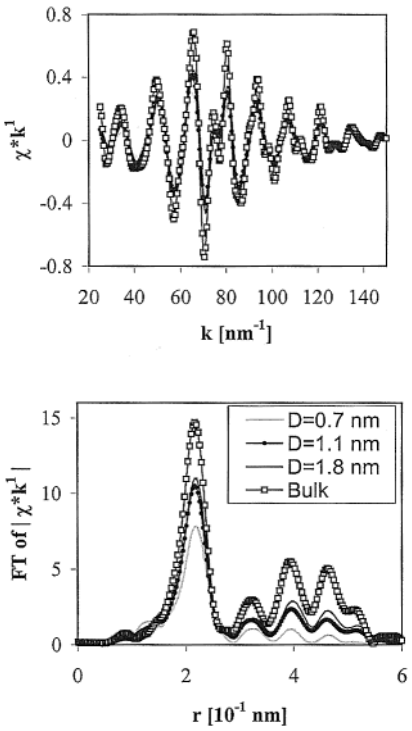

Figure 3. XAFS calculations on spherically truncated Ni clusters with various diameters, D. Upper diagram: XAFS signal. Lower diagram: k^1-weighted magnitude of Fourier transformed spectra.

The reduction of the overall intensity is again due to the small cluster size. The lower part of Figure 4 shows the data obtained at the Au L_3-edge. For the lowest concentrations of Au the spectra differ strongly from bulk Au (compare to Figure 2). This is due to the fact that the surrounding of the Au atoms mainly consists of Ni atoms (see MC simulations above).

3.3. TEM. A typical TEM image of the silica supported samples shows particle sizes in the range of 2.5−6.0 nm (Table 1 and Figure 5). The particles consist mainly of Ni as determined

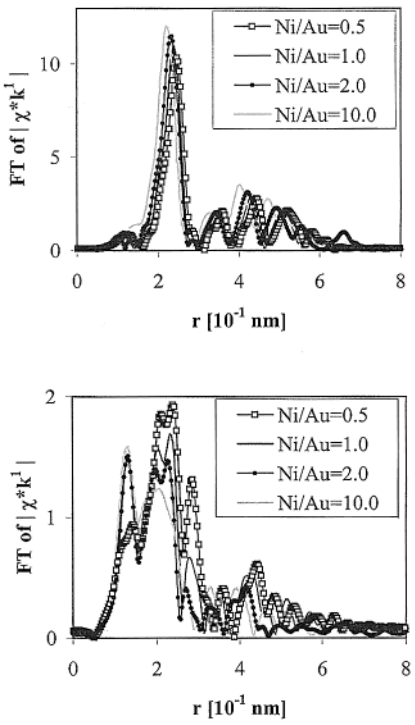

Figure 4. Magnitudes of the Fourier transformed XAFS spectra calculated on spherically truncated surface−alloy Ni−Au clusters with 249 atoms in total and several Ni/Au ratios. Upper part: data calculated at the Ni K-edge. Lower part: data calculated at the Au L_3-edge.

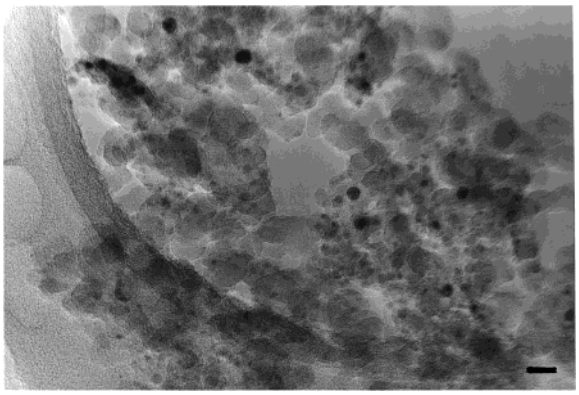

Figure 5. TEM photograph of a 5% Ni, 0.4% Au on SiO_2 sample (Sample 2). The width of the bar in the downright corner corresponds to 10 nm.

by elemental microanalysis. For the Ni−Au/SiO_2 catalysts, some 10−20 nm large particles are also observed which consist mainly of Au. The TEM images of the $MgAl_2O_4$ supported samples show particle sizes in the range of 3.0−15.0 nm (Table 2). Microanalysis of several tens of particles from the bimetallic catalysts shows that both Au and Ni are present in the same particles although the atomic ratio varies for the different particles.

3.4. XRPD. The X-ray diffractogram of the as-prepared silica supported Ni catalyst shows broad NiO lines on top of a large amorphous (silica from support and quartz from the capillary tube) background (Figure 6a). The diagram of the as-prepared silica supported Ni−Au catalyst is very similar to that of the as-prepared Ni−SiO_2 catalyst but shows in addition lines characteristic for metallic Au. The average crystallite size of the Au phase as calculated from the half-width of the Au[111] line is 8.2 ± 1 nm. Upon exposure to hydrogen at high temperature the NiO phase is reduced to metallic Ni (Figure

TABLE 2: Results of Fitting the First Shell Back-Transformed Spectra at the Ni K-Edge of Ni and Ni−Au Supported Catalysts after Reduction in Hydrogen To Amplitude and Phase Functions Obtained from a Ni Reference Foil[a]

sample	N_{Ni}	R_{Ni} [10^{-1} nm]	σ_{Ni} [10^{-3} nm]	ΔE_{Ni} [eV]	χ^2
			k^{-1}		
1	10.0	2.518	7.5	−1.2	3.6×10^{-3}
2	10.2	2.512	8.2	−3.3	6.0×10^{-3}
4	10.6	2.530	8.3	−0.2	5.4×10^{-3}
5	8.4	2.519	7.2	−1.5	4.4×10^{-3}
6	8.8	2.522	7.1	−1.2	8.4×10^{-3}
Ni foil	12	2.492	7.3		
			k^3		
1	10.5	2.520	0.077	−1.6	8.5
2	9.6	2.518	0.077	−1.5	49.2
4	10.2	2.530	0.081	−0.2	34.1
5	7.9	2.518	0.069	−1.3	38.8
6	8.6	2.518	0.070	−0.6	33.2

[a] Fit results are given for the EXAFS functions weighted with factors k^1 and k^3 in the k range 25−150 nm^{-1}. The first shell was chosen as the r range 0.12−0.29 nm.

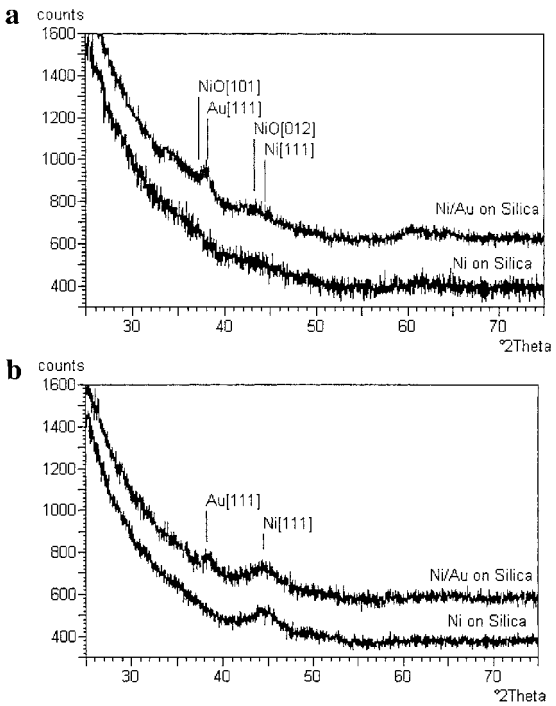

Figure 6. (a, upper part) Part of the XRPD diagrams of the as-prepared silica supported Ni (Sample 1, lower diagram) and Ni−Au (Sample 2, upper diagram) catalysts collected at room temperature. The positions of the bulk Au[111], Ni[111], NiO[101] and NiO[012] diffraction lines are indicated. (b, lower part) Part of the XRPD diagrams of the silica supported Ni (Sample 1, lower diagram) and Ni−Au (Sample 2, upper diagram) catalysts collected in situ after reduction in hydrogen. The positions of the bulk Au[111] and Ni[111] diffraction lines are indicated.

6b). For both the Ni−SiO_2 and the Ni−Au−SiO_2 catalyst, the Ni crystallite size as estimated from the width of the Ni[111] line is 3.3 ± 0.2 nm. The Au crystallite size does not change significantly upon reduction of the catalyst. The sizes, as calculated here, are average crystallite sizes perpendicular to the [111] direction for crystallites in the detection range of XRPD, i.e., crystallites below about 2 nm do not contribute to the peak intensity but are lost in the background signal.

The diffractograms of the as-prepared Ni−Au−$MgAl_2O_4$ catalysts show distinct diffraction lines from the support: $MgAl_2O_4$ and α-Al_2O_3 and from NiO, Ni, and possibly Au

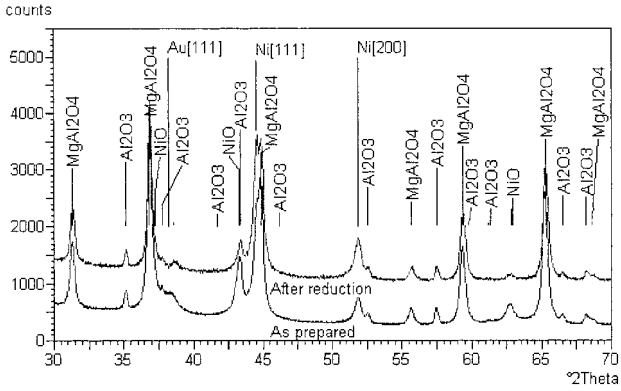

Figure 7. Part of the XRPD diagrams of the spinel supported Ni−Au catalysts collected on the as-prepared sample (Sample 7, lower diagram) and in situ on the sample after reduction in hydrogen (upper diagram). The positions of the bulk $MgAl_2O_4$, Al_2O_3, and NiO diffraction lines, as well as those of the bulk Au[111], Ni[111], and Ni[200] diffraction lines, are indicated.

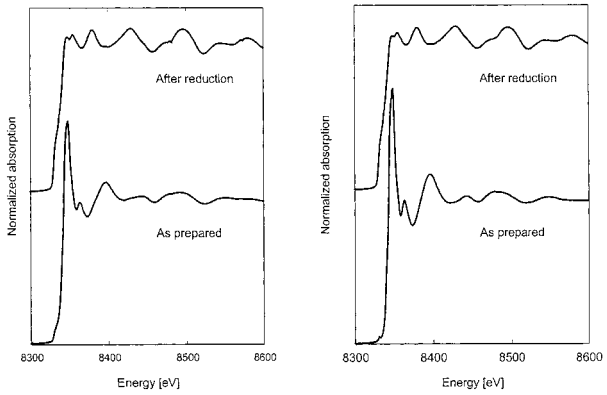

Figure 8. Normalized EXAFS spectra collected at the Ni K-edge, for the as-prepared samples and after reduction in a hydrogen flow. All spectra were measured at room temperature. Left: Ni on silica (Sample 1). Right: Ni−Au on silica (Sample 2).

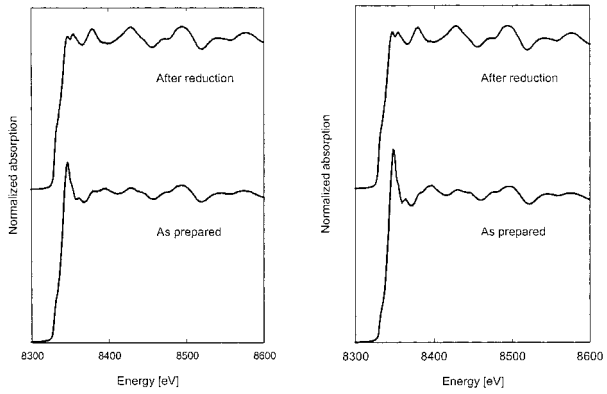

Figure 9. Normalized EXAFS spectra collected at the Ni K-edge, for the as-prepared samples and after reduction in a hydrogen flow. All spectra were measured at room temperature. Left: Ni on $MgAl_2O_4$ (Sample 5). Right: Ni−Au on $MgAl_2O_4$ (Sample 6).

(Figure 7). After reduction, both catalysts show metallic Ni with an average crystallite size of 17 ± 1 nm. A small amount of NiO is still present, indicating incomplete reduction under the conditions applied. No lines from a Au phase can be observed in the bimetallic catalyst after reduction.

3.5. EXAFS Measurements. EXAFS spectra were collected on the silica and spinel supported Ni and Ni−Au catalysts in the as-prepared state and after reduction (Figures 8 and 9). The Ni K-edge EXAFS spectra of the as-prepared catalysts are

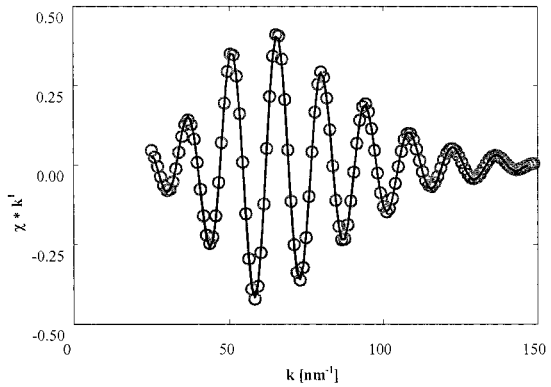

Figure 10. k^1-weighted EXAFS function of the nearest-neighbor shell contribution at the Ni K-edge for the silica supported Ni sample (Sample 1), after reduction in hydrogen. The circles represent the Fourier-backtransformed data and the solid curve is the fit to the data using Ni reference functions.

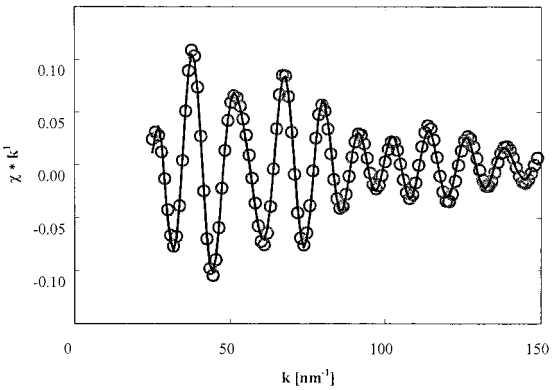

Figure 11. k^1-weighted EXAFS function of the nearest-neighbor shell contribution at the Au L_3-edge for the silica supported Ni−Au sample (Sample 2), after reduction in hydrogen. The circles represent the Fourier back-transformed data and the solid curve is the fit to the data using both Au and Ni reference functions.

characteristic of NiO although the $MgAl_2O_4$ supported catalysts show a much less intense white line and somewhat different EXAFS oscillations compared to the silica supported catalysts. The samples were subsequently exposed to pure hydrogen and heated to 873 K while quick-EXAFS (QEXAFS) spectra were collected. From the decrease in the height of the white line, it can be concluded that, for the silica supported catalysts, about half of the Ni is transformed from oxidized to metallic Ni at about 493 K and for the Ni−Au catalyst at about 723 K. The white line has disappeared completely at about 873 K. For the catalysts supported on $MgAl_2O_4$ the reduction is shifted from 493 K on the pure Ni supported catalyst (Sample 5) to 593 K on the Ni−Au catalyst (Sample 6). Similar trends are found from analyzing the reduction of the height of the nearest neighbor oxygen peak in the Fourier transformed data. After reduction, the samples were cooled to room temperature in pure hydrogen and an EXAFS spectrum was collected (Figures 8 and 9). Fitting the back-transformed Ni K-edge data of the first coordination shell with amplitude and phase functions obtained from a Ni reference foil results in perfect fits for both the Ni and the Ni−Au catalyst after reduction. The results of the fitting procedure are listed in Table 2 and Figure 10 shows a typical fitted spectrum for the Ni−SiO_2 catalyst. The reduction of the coordination number with respect to the ideal bulk coordination is due to the relative small size of the Ni particles. Assuming a spherically truncated particle shape and no influences from anharmonic effects,[27] the coordination numbers correspond to diameters in the range of 2−4 nm in good agreement with the XRPD and the TEM measurements. Comparing the interatomic distances to the bulk Ni−Ni distance, it can be seen that the interatomic distance in the catalyst particles is expanded by approximately 1%. The fact that the back-transformed spectra obtained from the Ni−Au catalyst can be fitted assuming that Ni only has Ni neighbors shows that the majority of the Ni atoms has a local structure similar to bulk Ni.

Fitting the first shell back-transformed Au L_3-edge spectra of the as-prepared catalysts with Au and Ni reference functions gives rise to poor fits. This is most probably due to the presence of NiO in the fresh catalyst. First shell back-transformed spectra of reduced Ni−Au catalysts can only be fitted properly by including both Au and Ni neighbors around the absorbing Au atoms. Because of the lack of suitable reference samples, theoretical phase and amplitude functions for the Au−Ni absorber-scatterer pairs were generated from the FEFF 8.00 code. The (metastable) Ni_3Au alloy (spacegroup $Pm3m$, a = 0.3675 nm) was used as the model structure to calculate the reference functions. Figure 11 shows an example of the fitting of the back-transformed Au L_3 spectrum of a silica supported Ni−Au catalyst (Sample 2). The fit results are listed in Table 3. The nonzero value of the Au−Ni coordination number gives evidence for the presence of Ni in the nearest neighbor environment of Au. However, the Au−Au coordination number is larger than what can be expected for a Au surface alloy. Here we have to take into account that XAFS probes all Au present in the sample, also Au present as large Au particles as evidenced by TEM and XRPD results.

To get a more detailed understanding of the XAFS spectra a direct comparison between measured and calculated XAFS spectra is performed in which the presence of large Au particles was taken into account as well. From the data collected at the Ni K-edge, the average size of the Ni particles can be estimated to be approximately 2−4 nm. Linear combinations of calculated Au L_3 XAFS functions of bulk Au and Au−Ni surface alloys were compared to the experimental data by varying the amount of Au on Ni in the particles as well as the relative amount of bulk Au. Figure 12 shows a comparison of the Fourier transformed spectra collected for the reduced silica supported Ni−Au catalyst and calculated XAFS spectra. The best-fit results in 73% of the Au present as bulk Au and the remainder of the Au present as a surface alloy (atomic ratio Ni/Au = 10.0) on a Ni particle with a diameter of 1.8 nm. Figure 12 shows a projected snapshot of the surface−alloy cluster as well. The Ni−Ni interatomic distance corresponded to the bulk Ni distance.

Comparison of the EXAFS spectra and the Fourier transformed data of the freshly reduced catalyst and the catalyst after steam reforming in diluted *n*-butane, shows no significant differences.

3.6. Reactivity of the Ni−Au Catalysts. From the mass spectrometry data for the *n*-butane concentration, the conversion was calculated and the results for the Ni−Au/$MgAl_2O_4$ and Ni−$MgAl_2O_4$ catalysts were shown previously.[16] Here it could be seen clearly that the mono-metallic Ni catalyst deactivated fast whereas the conversion of the Ni−Au catalyst remained essentially constant. Similar trends were observed for the silica-supported catalysts. In independent catalytic activity measurements it was found that the initial activity is smaller for the Ni−Au catalysts compared to the pure Ni catalysts.

3.7. Deactivation during Steam Reforming. Figure 13 shows the results of the TGA measurements for the spinel supported Ni and Ni−Au catalysts during steam reforming of *n*-butane. The open circles show the total weight increase for

TABLE 3: Results of Fitting the First Shell Back-Transformed Spectra at the Au L_3-Edge of Silica Supported Ni−Au Catalysts after Reduction in Hydrogen To Amplitude and Phase Functions Obtained from a Au and Ni Reference Foils[a]

sample	N_{AuAu}	N_{AuNi}	R_{auAu} [10^{-1} nm]	R_{AuNi} [10^{-1} nm]	σ_{AuAu} [10^{-3} nm]	σ_{AuNi} [10^{-3} nm]	ΔE_{AuAu} eV]	ΔE_{AuNi} [eV]	χ^2
					k^1				
2	7.1	0.8	2.882	2.428	8.3	8.1	0.0	−5.6	2.4×10^{-3}
4	7.4	2.5	2.914	2.461	8.7	11.0	−1.0	−5.1	5.2×10^{-3}
Au foil	12		2.885		8.7		0		
					k^3				
2	6.5	0.9	2.870	2.428	8.0	8.0	2.3	−5.7	29
4	9.0	1.2	2.919	2.461	9.2	10.5	−2.2	−5.0	46
Au foil	12		2.885		8.7		0		

[a] Fit results are given for the EXAFS functions weighted with factors k^1 and k^3 in the k range 25−150 nm^{-1}. The first shell was chosen as the r range 0.15−0.35 nm.

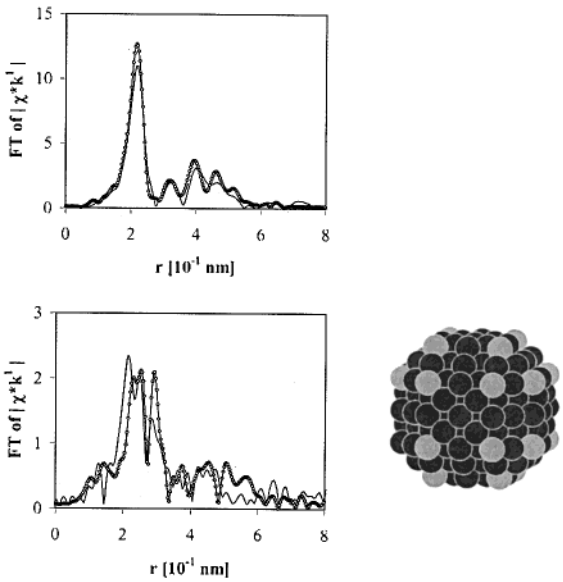

Figure 12. Comparison of the magnitudes of the k^1-weighted Fourier transformed XAFS spectra at the Ni K-edge (upper diagram) and Au L_3-edge (lower diagram). The reduced silica supported Ni−Au catalyst (Sample 2, solid curves) is compared to calculated spectra (curves with dots) obtained from a linear combination of calculated bulk Au spectra and calculated spectra of a Ni−Au surface alloy (see projected snapshot; Au atoms are light, Ni atoms are dark).

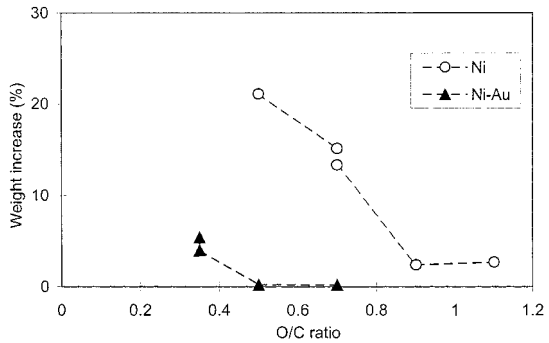

Figure 13. Weight increase of Ni−$MgAl_2O_4$ (Sample 5) and Ni−Au−$MgAl_2O_4$ (Sample 7) supported catalysts for several O/C ratios as measured by thermogravimetric analysis.

the Ni catalyst and the solid triangles show the results for the Ni−Au catalyst as a function of the O/C ratio at a temperature of 823 K. The amount of carbon deposition on the Ni−$MgAl_2O_4$ catalyst is significantly higher than that on the Ni−Au−$MgAl_2O_4$ catalyst. Under severe reforming conditions (i.e., low O/C ratios) the carbon deposition increases but is still negligible at O/C = 0.5 for the Ni−Au catalyst.

4. Discussion

The Monte Carlo simulations suggest that a surface alloy between Ni and Au also exists in Ni nanoparticles of sizes and compositions relevant for experimental catalysts. Au segregating to the surface of small Ni clusters was shown recently in a combined XPS, LEIS, TEM and Monte Carlo study of $Au_{0.5}Ni_{0.5}$ alloys.[28] The cluster beam deposition in combination with the carbon support used in that study resulted in a narrow size distribution of the bimetallic particles. The TEM measurements of our study of the Ni−Au catalysts show nanosized particles with an average size depending on the support. The fact that microanalysis studies show a Au signal associated with the Ni particles indicates that the two elements are in close proximity. In the silica supported catalysts large crystals of pure Au are also observed, indicating that not all of the Au is associated with the Ni. XRPD results support the existence of relatively large Au particles. The Ni particle sizes estimated by XRPD are in nice agreement with those determined by TEM for the smallest particles, i.e., the Ni−Au particles. The observation that separate particles of Au are present in the silica supported Ni−Au catalyst is interesting in view of the previous results[29] indicating that Au had no effect on the carbon deposition rate of a Ni catalyst. Presumably the preparation technique used in this study led to a bimetallic catalyst system in which the two elements were completely segregated.

The EXAFS results at the Ni K-edge are very similar for all the catalysts and show structural features of metallic nickel. Assuming a spherically truncated particle shape, the coordination numbers correspond to diameters in the range of 2−4 nm, in agreement with the XRPD and the TEM measurements. The 1% expansion of the Ni−Ni distance with respect to bulk Ni for both the pure Ni and the Ni−Au supported samples might be due to the interaction of the particles with the support. Because of the high Ni/Au ratio, it is not expected that the EXAFS spectra at the Ni K-edge are sensitive to the presence of Au in the Ni−Au catalysts. However, by tuning the X-rays to the Au L_3-edge it becomes possible to detect Ni neighbors in the nearest neighbor environment of Au. The EXAFS data at the Au L_3-edge show clear signs of alloying since the oscillations from the nearest neighbor contribution to the EXAFS are only possible to fit if Ni neighbors are included in addition to Au neighbors.

The comparison of measured data on bulk Au and Ni to calculated XAFS spectra gives confidence in the FEFF calculation code. The combination of XAFS calculations and the results of the Monte Carlo simulations was used to calculate XAFS spectra of Ni−Au surface−alloy particles. The direct comparison with experimental data (Figure 12) is not limited to the first shell data but includes the total local environment of Au and Ni atoms. The results show that about one-quarter of the

Au in the catalyst is present as a Ni−Au surface alloy, the rest being present in separate large Au particles. The agreement with the experimental data is less good than for the bulk samples due to the complex structure of the catalyst. Effects on the XAFS signals of particle size distribution and interactions with the substrate were not included in the model. Furthermore, the correlated Debye model used to calculate the Debye−Waller factors is most probably not very accurate for small clusters. Nevertheless the model of a combination of a surface alloy and bulk Au can describe the data reasonably well. The size of the surface−alloy cluster (1.8 nm) is in reasonable agreement with particle sizes obtained from TEM and average crystallite sizes obtained from XRPD.

Alloy formation in the Ni−Au bimetallic catalysts could also be detected in an indirect way by exposing the reduced catalysts to oxygen. Whereas the monometallic catalysts showed a strong increase in the white line at the Ni K-edge upon passivation, the Ni−Au catalysts only revealed a small increase. The difference is taken as supporting evidence for the presence of Au at the Ni surface since the Au is expected to make the Ni atoms in the surface more noble,[14] thus reducing their ability to oxidize.

The catalytic measurements performed simultaneously with the EXAFS measurements show that the monometallic Ni catalyst deactivates rather fast at the conditions applied. In contrast the Ni−Au catalysts are much more robust and show essentially no deactivation in good agreement with the predictions from the DFT calculations and the experimental surface science studies.[13,14] The deactivation of the Ni catalysts is attributed to deposition of carbon as also observed by the weight increase of the catalysts in the TGA investigations. In the latter studies the carbon deposition could only be observed in the monometallic catalysts for O/C ratios above 0.5. The Monte Carlo simulations revealed that Au atoms favor the edge and kink sites at the surface of the Ni particle. The presence of Au atoms at the low-coordination sites might give an indication for the mechanism of carbon formation. Adsorption of C atoms at the highly reactive edge and kink Ni sites might be blocked by Au atoms and thus prevent the formation of carbon whiskers. The total amount of Au present at the surface of the Ni particles needs only to be very small (a couple of percent of the total number of Ni surface atoms, see Figure 12), because only part of the edge and kink sites need to be blocked by Au.

It should be stressed that the simulations were carried out in a vacuum and without the presence of a support. However, the fact that the physicochemical experiments also strongly indicate that a surface alloy is formed between Ni and Au lends confidence to the results of the simulations.

The results as discussed above might seem in contradiction with results obtained on the Cu−Ni system. Here, it was observed that a small amount (1%) of Cu in a Cu−Ni sample promotes carbon formation.[30] Larger amounts of Cu (10%) reduce the rate of carbon formation with respect to pure Ni. On bimetallic Cu−Ni nano particles Cu segregates to the Ni surface at low temperatures. Cu atoms have, in contrast to Au atoms, a preference to be present on the flat terrace sites,[31] because Cu and Ni have a small size mismatch. Thus, Cu atoms will not block step and kink sites and will not reduce carbon formation (at low concentrations). The slight promotion of carbon formation for low Cu concentration[30] might be due to the presence of Cu in the Ni surface. At higher Cu concentrations part of the Cu might be present at step and kink sites as well and thus block some of the sites for carbon formation.

5. Conclusions

The existence of a surface alloy between Ni and Au in SiO_2 and $MgAl_2O_4$ supported catalysts is indicated by Monte Carlo simulations and experimentally verified using a combination of in situ X-ray absorption fine structure, transmission electron microscopy, and in situ X-ray powder diffraction. The interpretation of the EXAFS results was aided by comparing the data with XAFS calculations using the information from the simulations. The mass spectroscopy data show that the initial deactivation of the Ni−Au supported catalyst is significantly lower compared to a Ni monometallic catalyst. The Ni−Au catalysts hardly deactivate, whereas the pure Ni catalyst rapidly forms carbon and deactivates. Thus, the Ni−Au catalysts exhibiting the surface alloy are more resistant toward carbon formation than the pure Ni catalyst. The Au atoms appear to block the high reactivity edge and kink sites on the small Ni particles, and thus lower the probability of adsorbed carbon to form graphite and carbon whiskers. The preparation of the Ni−Au nanoparticle catalyst system was inspired by the detailed experimental and theoretical work to understand the alloying and the chemical reaction processes on single-crystal surfaces. The fact that the design succeeded gives us the hope that in future catalyst design may be based on a fundamental understanding of surface structures and their reactivity.

Acknowledgment. This work has been partly financed by the Danish Natural Science Research Council and DANSYNC. The Center for Atomic-scale Materials Physics (CAMP) is sponsored by the Danish National Research Foundation. We gratefully acknowledge HASYLAB at DESY, Hamburg for providing synchrotron beam time at the beamlines RÖMO II and BW1 and ESRF, Grenoble for providing synchrotron beam time at beamline BM29. We thank A. Filipponi and M. Borowski for their assistance at BM29. We thank J. Hyldtoft and H. Teunissen for the preparation of the catalyst samples, O. Sørensen for performing the TEM/EDS measurements, L.P. Nielsen for performing the TGA measurements, P.L. Hansen, G. Steffensen, and L.P. Nielsen for their assistance with the EXAFS measurements, and F. Besenbacher and I. Chorkendorff for valuable disscussions.

References and Notes

(1) Sinfelt, J. H. *Bimetallic Catalysts. Discoveries, Concepts, and Applications*; John Wiley & Sons: New York, 1983.

(2) Ponec, V. *Adv. Catal.* **1983**, *32*, 149.

(3) Lytle, F. W.; Via, G. H.; Sinfelt, J. H. In *Synchrotron Radiation Research*; Winick, H., Doniach, S., Eds.; Plenum: New York, 1980; Chapter 12.

(4) Prins, R.; Koningsberger, D. C. In *X-ray Absorption: Principles, Applications, Techniques of EXAFS, SEXAFS, and XANES*; Prins, R., Koningsberger, D. C., Eds.; Wiley & Sons: New York, 1988.

(5) Sinfelt, J. H. *J. Catal.* **1973**, *29*, 308.

(6) Sinfelt, J. H.; Lam, Y. L.; Cusumano, J. A.; Barnett, A. E. *J. Catal.* **1976**, *42*, 227.

(7) Massalski, T. B., Ed. *Binary Alloy Phase Diagrams*; Metals Park: Ohio, 1986.

(8) Nielsen, L. P.; Besenbacher, F.; Stensgaard, I.; Lægsgaard, E.; Engdahl, C.; Stoltze, P.; Jacobsen, K. W.; Nørskov, J. K. *Phys. Rev. Lett.* **1993**, *71*, 754.

(9) Nielsen, L. P. Ph.D. Thesis, University of Aarhus, Denmark, 1996.

(10) Boerma, D. O.; Dorenbos, G.; Wheatley, G. H.; Buck, T. M. *Surf. Sci.* **1994**, *307*−*309*, 674.

(11) Jacobsen, J.; Nielsen, L. P.; Besenbacher, F.; Stensgaard, I.; Lægsgaard, E.; Rasmussen, T.; Jacobsen, K. W.; Nørskov, J. K. *Phys. Rev. Lett.* **1995**, *75*, 489.

(12) Ruban, A. V.; Skriver, H. L.; Nørskov, J. K. *Phys. Rev. B* **1999**, *59*, 15990.

(13) Holmblad, P. M.; Larsen, J. H.; Chorkendorff, I. *J. Chem. Phys.* **1994**, *104*, 7289.

(14) Kratzer, P.; Hammer, B.; Nørskov, J. K. *J. Chem. Phys.* **1996**, *105*, 5595.

(15) Holmblad, P. M.; Larsen, J. H.; Chorkendorff, I.; Nielsen, L. P.; Besenbacher, F.; Lægsgaard, E.; Kratzer, P.; Hammer, B.; Nørskov, J. K. *Catal. Lett.* **1996**, *40*, 131.

(16) Besenbacher, F.; Chorkendorff, I.; Clausen, B. S.; Hammer, B.; Molenbroek, A. M.; Nørskov, J. K.; Stensgaard, I. *Science* **1998**, *279*, 1913.

(17) Hyldtoft, J.; Nørskov, J. K.; Clausen, B. S. Process for Steam Reforming of Hydrocarbons. U.S. Patent 5997835, 1999.

(18) Geus, J. W. *Preparation of Catalysts III*; Poncelet, G., Grange, P., Jacobs, P. A., Eds.; Elsevier: Amsterdam, **1983**, 1.

(19) Jacobsen, K. W.; Nørskov, J. K.; Puska, M. J. *Phys. Rev. B* **1987**, *35*, 7423.

(20) Jacobsen, K. W.; Stoltze, P.; Nørskov, J. K. *Surf. Sci.* **1996**, *366*, 394.

(21) Hansen, P. L.; Molenbroek, A. M.; Ruban, A. V. *J. Phys. Chem. B* **1997**, *101*, 1861.

(22) Rehr, J. J.; Mustre de Leon, J.; Zabinsky, S. I.; Albers, R. C. *J. Am. Chem. Soc.* **1991**, *113*, 5135.

(23) Ankudinov, A. L.; Ravel, B.; Rehr, J. J.; Conradson, S. D. *Phys. Rev. B*, **1998**, *58*, 7565.

(24) Clausen, B. S.; Steffensen, G.; Fabius, B.; Villadsen, J.; Feidenhans'l, R.; Topsøe, H. *J. Catal.* **1991**, *132*, 524.

(25) Clausen, B. S.; Topsøe, H. *Catal. Today* **1991**, *9*, 189.

(26) Lengeler, B.; Eisenberger, P. *Phys. Rev. B* **1980**, *21*, 4507.

(27) Clausen, B. S.; Gråbæk, L.; Topsøe, H.; Hansen, L. B.; Stoltze, P.; Nørskov, J. K.; Nielsen, O. H. *J. Catal.* **1993**, *141*, 368.

(28) Rousset, J. L.; Cadete Santos Aires, F. J.; Sekhar, B. R.; Mélinon, P.; Prevel, B.; Pellarin, M. *J. Phys. Chem. B* **2000**, *104*, 5430.

(29) Isar-Ul Haque, Ph.D. Thesis, University of New South Wales, Australia, 1990.

(30) Alstrup, I.; Tavares, M. T. *J. Catal.* **1993**, *139*, 513.

(31) Yang, L.; DePristo, A. E. *J. Catal.* **1994**, *148*, 575.